

# Motion of Wavefronts in Semiconductor Superlattices

A. Carpio <sup>1</sup>, L. L. Bonilla <sup>2</sup> and G. Dell'Acqua <sup>2</sup>

<sup>1</sup> *Departamento de Matemática Aplicada, Universidad Complutense, Madrid 28040, Spain*

<sup>2</sup> *Departamento de Matemáticas, Escuela Politécnica Superior, Universidad Carlos III de Madrid, Avenida de la Universidad 30, 28911 Leganés, Spain*

*Also: Unidad Asociada al Instituto de Ciencia de Materiales (CSIC)*

(November 1, 2018)

An analysis of wavefront motion in weakly coupled doped semiconductor superlattices is presented. If a dimensionless doping is sufficiently large, the superlattice behaves as a discrete system presenting front propagation failure and the wavefronts can be described near the threshold currents  $J_i$  ( $i = 1, 2$ ) at which they depin and move. The wavefront velocity scales with current as  $|J - J_i|^{\frac{1}{2}}$ . If the dimensionless doping is low enough, the superlattice behaves as a continuum system and wavefronts are essentially shock waves whose velocity obeys an equal area rule.

5.45.-a, 73.50.Fq, 73.63.-b, 73.40.-c, 82.40.-g

## I. INTRODUCTION

Semiconductor superlattices (SL) are unique nonlinear systems. Experimental evidence shows features of spatially discrete systems (multistability of roughly as many stationary states as SL periods due to formation of electric field domains [1]) in certain regimes of nonlinear charge transport in SL. In other regimes (self-sustained periodic and chaotic oscillations of the current [2]), SL behavior is more typical of continuous systems. These different properties may be described by discrete [3] or continuous balance equation models [4]. The continuum limit of discrete SL models has been used to understand important aspects of self-oscillations [5]. On the other hand, discrete models of SL share common characteristics with spatially discrete systems in other fields: most importantly, front propagation failure and front depinning [6].

Discrete systems describe physical reality in many different fields: propagation of nerve impulses along myelinated fibers [7,8], pulse propagation through cardiac cells [8], calcium release waves in living cells [9], sliding of charge density waves [10], superconductor Josephson array junctions [11], arrays of coupled diode resonators [12], motion of dislocations in crystals [13] and atoms adsorbed on a periodic substrate [14]. A distinctive feature of discrete systems (not shared by continuous ones) is the phenomenon of wavefront pinning: for values of a control parameter in a certain interval, wavefronts joining two different constant states fail to propagate [8]. When the control parameter surpasses a threshold, the wavefront depins and starts moving [6,7,10,13]. The existence of such thresholds is thought to be an intrinsically discrete fact, which is lost in continuum approximations. The characterization of propagation failure and front depinning in discrete systems is thus an important problem, which is still poorly understood despite the numerous inroads made in the literature [7,9,10,13].

Recently, several of us have proposed a theory of front

depinning and propagation failure in discrete reaction-diffusion (RD) systems [15]. This theory will be extended here to describe motion of wavefronts near depinning thresholds in discrete drift-diffusion (DDD) models of SL [16]. There are important differences between RD and SL systems. Let us consider a RD system depending on a parameter  $A$ , measuring how close we are to the continuum limit ( $A = 0$ ), and an external parameter ('the field'  $F$ ) such that wavefronts move for all values of  $F \neq 0$  in the continuum limit. In a generic RD system, there is always a pinning interval (wavefronts are stationary for  $F$  in the pinning interval) about  $F = 0$  no matter how close to the continuum limit we are. As we approach the continuum limit, the pinning interval shrinks to zero exponentially fast as  $A$  approaches zero: we then need exponential asymptotics (asymptotics beyond all orders) to describe what happens. In a SL, there are important differences: (i) the pinning interval disappears before we reach the continuum limit, and (ii) the continuum limit is described by hyperbolic equations and shock waves (no exponential asymptotics is needed).

Let us consider an infinitely long, sufficiently doped SL under constant current conditions. The current density plays the role of external field in the SL models and a dimensionless doping  $\nu$  plays the same role as the parameter  $A$ : the continuum limit is reached as  $\nu \rightarrow 0$ . For large values of  $\nu$ , we are in the strongly discrete limit and wavefronts are stationary (pinned) for currents on a certain pinning interval. If the current is smaller than the lowest limit of the interval,  $J_1(\nu)$ , the wavefront moves downstream, following the electron flow. For currents larger than the upper limit of the interval,  $J_2(\nu)$ , wavefronts move upstream, against the electron flow [6]. As the doping decreases, first  $J_2$  and then  $J_1$  (for even lower doping) disappear. This means that fronts are either stationary or move downstream below a first critical doping and they always move downstream below a second critical doping. Since the continuum limit corresponds to vanishing dimensionless doping, stationary fronts and fronts moving upstream are features of discrete SL, which are

lost in the continuum limit.

In contrast with the precipitous jumps and falls of charge and electric field in individual wells during wavefront motion, we will show that, for currents outside  $(J_1, J_2)$ , wavefronts are described by continuous profiles moving at a constant velocity. These profiles become sharper as the currents approach the threshold values  $J_i$ ; see Fig. 1. Exactly at these values, wavefront profiles cease to be continuous: a number of jump discontinuities open up, which results in propagation failure. We describe propagation failure by analyzing the behavior of several *active* wells which govern front motion. Our theory yields the front profile near threshold currents and a universal scaling of the front velocity for sufficiently large doping. Its performance worsens as the doping decreases and we approach the continuum limit. We will complement our approach by obtaining the velocity of wavefronts and their shape in this limit. Previously, these front profiles and velocities in the continuum limit were known only for models having no discrete diffusion [17], which is correct only for high enough voltage bias. For bias on the first plateau of the current–voltage characteristics, diffusivity cannot be ignored. Given that characterizing wavefronts at constant current is the key to analyze self-oscillations at constant voltage, the results in this paper could be useful to describe self-oscillations at low biases. This could be done in two limits: near the continuum limit  $\nu \ll 1$ , the results we have obtained for shock waves and monopoles can be used to characterize self-oscillations, either mediated by monopoles [5] or by dipoles [18], [19]. For larger  $\nu$ , our present theory paves the way to understanding self-oscillations in DDD or more general SL models.

The rest of the paper is as follows. We describe front propagation failure and front depinning for DDD SL models in Section II. The continuum limit of the model is analyzed in Section III. The resulting equations are those of the Kroemer model of the Gunn effect with zero diffusivity. Wavefronts are shock wave solutions of this model with a rigid tail region either to the right or left of the shock. The shock velocity must be obtained from the discrete model, which results in an equal-area rule rather different from that of the Gunn effect. Corrections to this rule are important for describing the self-oscillations and will be given here. Section IV contains our conclusions. Lastly, the Appendices are devoted to different technical matters.

## II. PROPAGATION FAILURE AND FRONT DEPINNING

In weakly coupled SL, (inter and intra-subband) scattering times are much shorter than well escape times, which in turn are much shorter than macroscopic times (period of self-oscillations). Then the dominant mechanism of vertical transport is sequential tunneling, only

the first subband of each well is appreciably occupied and the tunneling current across barriers is stationary [3]. Nonlinear phenomena seen in experiments can be described by discrete balance equations.

We count the barrier separating the injecting contact from the first well of the SL as the zeroth barrier. Barriers and wells have widths  $d$  and  $w$ , respectively, so that  $l = d + w$  is the SL period. The  $i$ th SL period starts just before the  $i$ th barrier and ends just before the  $(i + 1)$ st barrier. With this convention, the dependent variables of our model are *minus* the electric field averaged over the  $i$ th period,  $F_i$ , and the two-dimensional electron density at the  $i$ th well (concentrated in a plane normal to the growth direction, located at the end of the  $i$ th well),  $n_i$ . These variables obey the Poisson and charge continuity equations:

$$F_i - F_{i-1} = \frac{e}{\varepsilon} (n_i - N_D^w). \quad (1)$$

$$\frac{dn_i}{dt} = J_{i-1 \rightarrow i} - J_{i \rightarrow i+1}. \quad (2)$$

Here  $N_D^w$ ,  $\varepsilon$ ,  $e$  and  $eJ_{i \rightarrow i+1}$  are the 2D doping density at the  $i$ th well, the average permittivity of the SL, minus the electron charge and the tunneling current density across the  $i$ th barrier, respectively. We can differentiate (1) with respect to time and eliminate  $n_i$  by using (2). The result can be written as a form of Ampère’s law for the balance of current

$$\frac{\varepsilon}{e} \frac{dF_i}{dt} + J_{i \rightarrow i+1} = J(t). \quad (3)$$

Here  $eJ(t)$  is the total current density through the SL, equal for all SL periods, and  $\varepsilon dF_i/dt$  is the displacement current at the  $i$ th SL period.

The tunneling current density  $eJ_{i \rightarrow i+1}$  is related to electric fields and electron densities by a *constitutive relation*, which should be derived from first principles; see Wacker in Ref. [3] and Ref. [16]. At sufficiently low or high temperatures,  $J_{i \rightarrow i+1}$  has the following drift-diffusion form [16],

$$J_{i \rightarrow i+1} = \frac{n_i v(F_i)}{l} - D(F_i) \frac{n_{i+1} - n_i}{l^2}, \quad (4)$$

where the *drift* velocity is an odd function of the field,  $v(-F) = -v(F)$ , and the *diffusion coefficient* satisfies the relation

$$D(-F) = v(F)l + D(F). \quad (5)$$

Typical forms of these coefficients (in nondimensional form; see below) are shown in Figure 2. To compare our theoretical results with numerical solutions of the model, it is better to use analytical approximations of these functions. Ours are given in Appendix A. The Ampère’s law corresponding to the current (4) is

$$\frac{\varepsilon}{e} \frac{dF_i}{dt} + \frac{n_i v(F_i)}{l} - D(F_i) \frac{n_{i+1} - n_i}{l^2} = J(t). \quad (6)$$

Equations (1) and (6) form the DDD model [6,16], studied here. Notice that for high fields (in practice for all plateaus except the first one),  $D = 0$ , and we have a simpler discrete drift model with  $J_{i \rightarrow i+1} = n_i v(F_i)/l$  [3].

To analyze the discrete drift-diffusion model, it is convenient to render all equations dimensionless. Let  $v(F)$  reach its first positive maximum at  $(F_M, v_M)$ . We adopt  $F_M$ ,  $N_D^w$ ,  $v_M$ ,  $v_M l$ ,  $eN_D^w v_M/l$  and  $\varepsilon F_M l / (eN_D^w v_M)$  as the units of  $F_i$ ,  $n_i$ ,  $v(F)$ ,  $D(F)$ ,  $eJ$  and  $t$ , respectively. For the first plateau of the 9/4 SL of Ref. [2], we find  $F_M = 6.92$  kV/cm,  $N_D^w = 1.5 \times 10^{11}$  cm $^{-2}$ ,  $v_M = 156$  cm/s,  $v_M(d+w) = 2.03 \times 10^{-4}$  cm $^2$ /s and  $eN_D^w v_M / (d+w) = 2.88$  A/cm $^2$ . The units of current and time are 0.326 mA and 2.76 ns, respectively. Then (1) and (6) become

$$\frac{dE_i}{dt} + v(E_i) n_i - D(E_i) (n_{i+1} - n_i) = J, \quad (7)$$

$$E_i - E_{i-1} = \nu (n_i - 1), \quad (8)$$

or, equivalently,

$$\frac{dE_i}{dt} + v(E_i) \frac{E_i - E_{i-1}}{\nu} - D(E_i) \frac{E_{i+1} + E_{i-1} - 2E_i}{\nu} = J - v(E_i). \quad (9)$$

Here we have used the same symbols for dimensional and dimensionless quantities except for the electric field ( $F$  dimensional,  $E$  dimensionless).  $\nu = eN_D^w / (\varepsilon F_M)$  is the dimensionless doping parameter, which is about 3 for the first plateau of the 9/4 SL.

### A. Phase diagram for wavefronts on an infinite superlattice

Here we shall consider an infinite SL under constant current bias  $J$ . Clearly, there are two stable spatially homogeneous stationary solutions, namely  $E^{(1)}(J)$  and  $E^{(3)}(J)$ , where  $v(E^{(k)}) = J$ ,  $E^{(1)}(J) < E^{(2)}(J) < E^{(3)}(J)$ . We are interested in nonuniform front states of the DDD model which satisfy  $E_i \rightarrow E^{(1)}(J)$  as  $i \rightarrow -\infty$  and  $E_i \rightarrow E^{(3)}(J)$  as  $i \rightarrow \infty$ . These states are either stationary or time-dependent. In the second case, they are wavefronts moving with constant velocity  $c = c(J, \nu)$ , such that  $E_i(t) = E(i - ct)$ ,  $i = 0, \pm 1, \dots$ .  $E(\tau)$  is a smooth profile which solves the following nonlinear eigenvalue problem for  $c$  (measured in wells traversed per unit time) and  $E(\tau)$ :

$$c \frac{dE}{d\tau} = v(E) - J + v(E) \frac{E - E(\tau - 1)}{\nu} - D(E) \frac{E(\tau + 1) + E(\tau - 1) - 2E}{\nu}, \quad (10)$$

$$E(-\infty) = E^{(1)}(J), \quad E(\infty) = E^{(3)}(J). \quad (11)$$

By using a comparison principle [20], we can prove the existence of stationary fronts rigorously [6]. Outside the

interval of current values in which there are stationary fronts, we can only prove that there are fronts moving to the right or the left [6]. By using the comparison principle, it is possible to show that moving and stationary fronts cannot exist simultaneously at the same value of the current [21]. This result does not hold if the spatially discrete differential equation is second order in time: moving and stationary fronts have been reported to coexist in one such case [22].

Proofs that moving fronts are traveling wavefronts have been given for different spatially discrete models without convection [23,21]. In the case of the DDD SL model, we rely on numerical evidence: Notice that all noticeable steps in Fig. 1, particularly (a) and (c), are of the same length. Fig. 3 shows the wavefront at three different times, and it clearly demonstrates that the front is a traveling wave moving with constant velocity as a whole. Our asymptotic construction of the wavefronts near the critical currents  $J_1$  and  $J_2$ , which we explain below, exploits their traveling wave nature.

Solving numerically (9), it can be shown that, after a short transient, a variety of initial conditions such that  $E_i \rightarrow E^{(1)}(J)$  as  $i \rightarrow -\infty$  and  $E_i \rightarrow E^{(3)}(J)$  as  $i \rightarrow \infty$  evolve towards either a stationary or moving monopole. Figure 3 of Ref. [6] is a phase diagram showing the regions in the plane  $(J, \nu)$  where different fronts are stable. There are two important values of  $\nu$ ,  $\nu_1 < \nu_2$ , such that:

- For  $0 < \nu < \nu_1$  and each fixed  $J \in (v_m, 1)$ , only traveling monopole fronts moving downstream (to the right) were observed. For  $\nu > \nu_1$ , stationary monopoles were found.
- For  $\nu_1 < \nu < \nu_2$ , traveling fronts moving downstream exist only if  $J \in (v_m, J_1(\nu))$ , where  $J_1(\nu) \in (v_m, 1)$  is a critical value of the current.  $J_1(\nu)$  is a monotone decreasing function such that  $J_1 \rightarrow v_m$  as  $\nu \rightarrow \infty$ ; see Fig. 4. If  $J \in (J_1(\nu), 1)$ , the stable solutions are steady fronts (stationary monopoles).
- New solutions are observed for  $\nu > \nu_2$ . As before, there are traveling fronts moving downstream if  $J \in (v_m, J_1(\nu))$ , and stationary monopoles if  $J \in (J_1(\nu), J_2(\nu))$ ,  $J_2(\nu) < 1$  is a new critical current; see Fig. 4. The function  $J_2(\nu)$  starts at  $J_2(\nu_2) = 1$ , decreases to a single minimum value, and then it increases towards 1 as  $\nu \rightarrow \infty$ . For  $J_2(\nu) < J < 1$ , the stable solutions of (12) and (13) are monopoles traveling upstream (to the left). As  $\nu$  increases,  $J_1(\nu)$  and  $J_2(\nu)$  approach  $v_m$  and 1, respectively. Thus stationary solutions are found for most values of  $J$  if  $\nu$  is large enough.

Wavefront velocity as a function of current has been depicted in Figure 5 for  $\nu = 3$ , which corresponds to the first plateau of the 9/4 SL. For larger  $\nu$ , the interval of  $J$  for which stationary solutions exist becomes wider again, trying to span the whole interval  $(v_m, 1)$  as  $\nu \rightarrow \infty$ . For very large  $\nu$ , the velocities of downstream and upstream

moving monopoles become extremely small in absolute value.

### B. Pinning of wavefronts with a single active well

At the critical currents,  $J_1(\nu)$  and  $J_2(\nu)$ , wavefronts moving downstream (to the right, following the electron flow,  $c > 0$ ) for smaller  $J$  or upstream (to the left, against the electron flow,  $c < 0$ ) for larger  $J$  fail to propagate. What happens is that the wavefront field profile  $E(\tau)$  becomes sharper as  $J$  approaches the critical currents. Exactly at  $J_k$ ,  $k = 1, 2$ , gaps open up in the wavefront profile which therefore loses continuity. The resulting field profile is a stationary front  $E_i = E_i(J, \nu)$ : the wavefront is pinned for  $J_1 < J < J_2$ . The depinning transition (from stationary fronts to moving wavefronts) is technically speaking a global saddle-node bifurcation. We shall study it first in the simplest case of large dimensionless doping  $\nu$ , and then indicate what happens in the general case.

For sufficiently large doping and  $J$  close to critical, the moving front is led by the behavior of a single well, which we will call the *active well*. If we examine the shape of a stationary front near the critical current, we observe that all wells are close either to  $E^{(1)}(J)$  or  $E^{(3)}(J)$  except for one well which drifts slowly and eventually jumps: the active well. Let us call  $E_0$  the electric field at the active well. Since all wells in the front perform the same motion, we can reconstruct the profile  $E(i - ct)$  from the time evolution of  $E_0(t) = E(-ct)$ . Before the active well jumps,  $E_i \approx E^{(1)}(J)$  for  $i < 0$  and  $E_i \approx E^{(3)}(J)$  for  $i > 0$ . Thus Eq. (9) becomes

$$\frac{dE_0}{dt} \approx J - v(E_0) - v(E_0) \frac{E_0 - E^{(1)}}{\nu} + D(E_0) \frac{E^{(1)} + E^{(3)} - 2E_0}{\nu}. \quad (12)$$

This equation has three stationary solutions for  $J_1 < J < J_2$ , two stable and one unstable, and only one stable stationary solution otherwise. At the critical currents, two of these solutions coalesce forming a saddle-node. At low values of the current, the two coalescing solutions form a double zero corresponding to a maximum of the right side of (12). For high currents, the two coalescing solutions form a double zero corresponding to a minimum of the right side of (12). The critical currents are such that the expansion of the right hand side of (12) about the two coalescing stationary solutions,

$$J - v(E_0) - v(E_0) \frac{E_0 - E^{(1)}}{\nu} + D(E_0) \frac{E^{(1)} + E^{(3)} - 2E_0}{\nu} = 0, \quad (13)$$

has zero linear term,

$$D'_0(E^{(1)} + E^{(3)} - 2E_0) - 2D_0 - v'_0(E_0 - E^{(1)}) - v_0 - \nu v'_0 = 0. \quad (14)$$

Here  $D'_0$  means  $D'(E_0)$ , etc. Equations (13) and (14) yield approximations to  $E_0$  and the critical current  $J_c$  (which is either  $J_1$  or  $J_2$ ). The results are depicted in Figs. 5 and 6, and show excellent agreement with those of numerical solutions of the model for  $\nu > 2$ . Our approximation performs less well for smaller  $\nu$ , which indicates that more active wells are needed to improve it.

Let us now construct the profile of the traveling wavefronts after depinning, for  $J$  slightly below  $J_1$  or slightly above  $J_2$ . Up to terms of order  $|J - J_c|$ , Equation (12) becomes

$$\frac{d\varphi}{dt} \approx \alpha(J - J_c) + \beta\varphi^2, \quad (15)$$

for  $E_0(t) = E_0(J_c) + \varphi(t)$ , as  $J \rightarrow J_c$ .  $E_0(J_c)$  is the stationary solution of (12) at  $J = J_c$ . The coefficients  $\alpha$  and  $\beta$  are given by

$$\alpha = 1 + \frac{v_0 + D_0}{\nu v'_1} + \frac{D_0}{\nu v'_3}, \quad (16)$$

$$2\nu\beta = D''_0(E^{(1)} + E^{(3)} - 2E_0) - 4D'_0 - 2v'_0 + v''_0(E^{(1)} - E_0 - 2\nu). \quad (17)$$

$\beta$  is negative if  $J_c = J_1$  and positive if  $J_c = J_2$ . Eq. (15) has the (outer) solution

$$\varphi(t) \sim (-1)^k \sqrt{\frac{(\alpha(J - J_k))}{\beta}} \tan\left(\sqrt{\alpha\beta(J - J_k)}(t - t_0)\right) \quad (18)$$

( $k = 1, 2$ ), for  $J$  such that  $\text{sign}(J - J_k) = \text{sign}\beta$ . (18) is very small most of the time, but it blows up when the argument of the tangent function approaches  $\pm\pi/2$ . Thus the outer approximation holds over a time interval  $(t - t_0) \sim \pi/\sqrt{\alpha\beta(J - J_k)}$ . The reciprocal of this time interval yields an approximation for the wavefront velocity,

$$|c(J, \nu)| \sim \frac{\sqrt{\alpha\beta(J - J_k)}}{\pi}. \quad (19)$$

In Figs. 5 and 6, we compare this approximation with the numerically computed velocity for  $\nu = 3$  and  $\nu = 20$ , respectively.

When the solution begins to blow up, the outer solution (18) is no longer a good approximation, for  $E_0(t)$  departs from the stationary value  $E_0(J_c)$ . We must go back to (12) and obtain an inner approximation to this equation. As  $J$  is close to  $J_c$  and  $E_0(t) - E_0(J_c)$  is of order 1, we solve numerically (15) at  $J = J_c$  with the matching condition that  $E_0(t) - E_0(J_c) \sim (-1)^k 2/[\pi\sqrt{\beta}/[\alpha(J - J_c)] - 2|\beta|](t - t_0)$ , as  $(t - t_0) \rightarrow -\infty$ . This inner solution describes the jump of  $E_0$  to values close to  $E^{(1)}$  if  $J_c = J_1$ , or to values close to  $E^{(3)}$

if  $J_c = J_2$ . During this jump, the motion of  $E_0$  forces the other points to move. Thus, for  $J_c = J_1$ ,  $E_1(t)$  can be calculated by using the inner solution in (9) for  $E_0$ , with  $J = J_c$  and  $E_2 \approx E^{(3)}$ . Similarly, for  $J_c = J_2$ ,  $E_{-1}(t)$  can be calculated by using the inner solution in (9) for  $E_0$ , with  $J = J_c$  and  $E_{-2} \approx E^{(1)}$ . A composite expansion [24] constructed with these inner and outer solutions is compared to the numerical solution of the model in Fig. 7. Notice that we have reconstructed the traveling wave profiles  $E(i - ct)$  from the identity  $E_0(t) = E(-ct)$ .

### C. Pinning of wavefronts with several active wells

The previous asymptotic description of the depinning transition deteriorates as  $\nu$  decreases. What happens is that we need more than one active well to approximate wavefront motion. Depinning is then described by a reduced system of more than one degree of freedom corresponding to active wells. There is a saddle-node bifurcation in this reduced system whose normal form is again (15) with different coefficients. The jump of the active wells after blow up is found by solving the reduced system with a matching condition. How do we determine the optimal number of active wells? For a given  $\nu$ , the eigenvector corresponding to the zero eigenvalue has a certain number of components that are of order one, whereas all others are very small. The number of components of normal size determines the optimal number of active wells: only one well if  $\nu$  is larger than 10, four if  $\nu = 3$ , etc. The eigenvector of the reduced system of equations for the active wells is a good approximation to the large components of the eigenvector corresponding to the complete system. As we approach the continuum limit, more and more points enter the reduced system of equations and the approach of Section III becomes a viable alternative to these methods.

As before, the wavefront profile will obey  $E(i - ct) = E_i(t)$ , where  $i = -L, \dots, M$  are the indices of the  $A = L + M + 1$  active wells. Then their reduced dynamics obeys (9) for  $i = -L, \dots, M$  together with the approximations  $E_{-L-1} \sim E^{(1)}$  and  $E_{M+1} \sim E^{(3)}$ . We have to find approximate stationary solutions of this system, and then linearize it with respect to the appropriate one. At the approximate critical current  $J_c$ , one of the eigenvalues of the linearized system becomes zero. Let us call  $U_i^\dagger$  and  $U_i$  the  $A$ -dimensional ( $A = L + M + 1$ ) left and right eigenvectors corresponding to the zero eigenvalue of the coefficient matrix for the linearized system, chosen so that  $\sum_{i=-L}^M U_i^\dagger U_i = 1$ . Very close to  $J_c$ , the electric field profile will be  $E_i(t) \sim E_i(J_c, \nu) + U_i \varphi(t)$  plus terms which decrease exponentially fast as time elapses.  $\varphi$  obeys Eq. (15) with the following coefficients

$$\alpha = \sum_{i=-L}^M U_i^\dagger + \frac{v_0 + D_0}{\nu v'_{-L-1}} U_0^\dagger + \frac{D_M U_M^\dagger}{\nu v'_{M+1}}, \quad (20)$$

$$\beta = \frac{1}{2\nu} \sum_{i=-L}^M [D_i'' U_i^2 (E_{i+1} + E_{i-1} - 2E_i) + 2D_i' U_i (U_{i+1} + U_{i-1} - 2U_i) - 2v_i' U_i (U_i - U_{i-1}) + v_0'' (E_{i-1} - E_i - 2\nu) U_i^2] U_i^\dagger. \quad (21)$$

Here we have set  $U_{-L-1} = U_{M+1} = 0$ ,  $E_{-L-1} = E^{(1)}$ ,  $E_{M+1} = E^{(3)}$ ,  $v_i = v(E_i)$ ,  $v_i' = v'(E_i)$ ,  $D_i = D(E_i)$ , etc. All quantities are evaluated at  $J = J_c$ . Clearly these formulas become (16) and (17) if  $L = M = 0$ ,  $U_0 = U_0^\dagger = 1$ .

Obviously, the solution and interpretation of (15) is the same as before, and we only have to change the matching condition and the description of the jump of the active wells. Increasing the number of active wells improves appreciably the approximation of the wavefront velocity; see Fig. 5. The jump of the active wells is described by the solution of (9) for  $i = -L, \dots, M$ , with  $J = J_c$ ,  $E_i(t) = E_i(J_c, \nu) + U_i \varphi(t)$ , and the same matching condition as before. Fig. 8 depicts a comparison of the composite approximation and the numerically calculated field profile for  $\nu = 3$ . Notice the improvement with respect to the single active well approximation.

Our analysis shows that the transition from moving to stationary fronts involves loss of continuity of the wavefront profile. For the reduced system of active wells, the transition is a global saddle-node bifurcation: two stationary solutions coalesce at the critical current and (for  $J < J_1(\nu)$  or  $J > J_2(\nu)$ ), a traveling wavefront appears. Near the critical currents, the field profile of this front is very sharp: it resembles the typical discrete steps of the stationary profile on long intervals of time (scaling as  $|J - J_i|^{-\frac{1}{2}}$ ), followed by abrupt transitions between steps. Although we do not have a proof, it is natural to conjecture that the depinning transition for the complete SL model is of the same type as that for the reduced system of active wells.

*Remark.* Notice that our theory of front depinning applies with minor modifications to discrete models with more complicated (than (4)) constitutive relations,  $J_{i \rightarrow i+1} = \mathcal{J}(F_i, n_i, n_{i+1})$  (cf Wacker's paper in Ref. [3]) or  $J_{i \rightarrow i+1} = \mathcal{J}(F_{i-1}, F_i, F_{i+1}, n_i, n_{i+1})$  (cf the complete discrete model in Ref. [16] where potential drops at the barriers,  $V_i$ , are used instead of electric fields averaged over one SL period,  $F_i$ ). The key point is that only a finite number of wells are active in wavefront depinning for sufficiently large  $\nu$ .

### III. CONTINUUM LIMIT

The continuum limit of the DDD model is useful to understand self-sustained oscillations of the current and wavefront motion. It consists of  $\nu \rightarrow 0$ ,  $i \rightarrow \infty$ , with  $\nu i = x \in [0, N\nu]$ ,  $N\nu \gg 1$ . In this limit, (9) becomes

$$\frac{\partial E}{\partial t} + v(E) \frac{\partial E}{\partial x} = J - v(E), \quad (22)$$

up to terms of order  $\nu$ . Equation (22) corresponds to the hyperbolic limit of the well-known Kroemer model of the Gunn effect [18]. With constant  $J$ , shock waves are solutions of these equations [25]. These waves are related to wavefronts, and their speed can be calculated explicitly. Let  $V(E_+, E_-)$  denote the speed of a shock wave such that  $E$  becomes  $E_-$  (resp.  $E_+$ ) to the left (resp. right) of the shock. Inside the shock wave, we should use the discrete model with  $n_i \gg 1$ ,  $dE_i/dt \sim -V(E_i - E_{i-1})/\nu \gg 1$ , and  $J = O(1)$ . Notice that we have rescaled the wavefront velocity so that  $V = c\nu$  is the correct velocity for the (rescaled) continuum profile  $E(x - Vt) = E(\nu(i - ct))$ . Then

$$\begin{aligned} E_+ - E_- &= \sum (E_i - E_{i-1}) \sim \nu \sum n_i \\ &\sim V \sum \frac{E_i - E_{i-1}}{v(E_i) + D(E_i)} + \sum \frac{D(E_i)}{v(E_i) + D(E_i)} \nu n_{i+1} \\ &\sim V \sum \frac{E_i - E_{i-1}}{v(E_i) + D(E_i)} + \sum \frac{D(E_i)(E_{i+1} - E_i)}{v(E_i) + D(E_i)}. \end{aligned}$$

This expression yields

$$V \sim \frac{\sum \frac{v(E_i)(E_{i+1} - E_i)}{v(E_i) + D(E_i)}}{\sum \frac{E_i - E_{i-1}}{v(E_i) + D(E_i)}},$$

which becomes

$$V(E_+, E_-) = \frac{\int_{E_-}^{E_+} \frac{v(E)}{v(E) + D(E)} dE}{\int_{E_-}^{E_+} \frac{dE}{v(E) + D(E)}}, \quad (23)$$

in the continuum limit. This expression is equivalent to the following weighted equal-area-rule

$$\int_{E_-}^{E_+} \frac{v(E) - V(E_+, E_-)}{v(E) + D(E)} dE = 0. \quad (24)$$

For  $D = 0$ , this formula reduces to that derived for the discrete drift model in Ref. [17]. An expression including the next correction to this formula is given in Appendix B. There is only one value of  $J$ ,  $J^*$ , such that  $V = J$  with  $E_- = E^{(1)}(J)$  and  $E_+ = E^{(3)}(J)$ . For  $J \in (v_m, J^*)$ , a wavefront joining  $E^{(1)}(J)$  to  $E^{(3)}(J)$  consists of a shock wave having  $E_+ = E^{(3)}(J)$ , and  $E_-$  such that  $V(E^{(3)}(J), E_-) = v(E_-)$ . Furthermore, to the left of the shock wave, there is a *tail* region moving rigidly with the shock and such that

$$[v(E) - V] \frac{\partial E}{\partial \xi} = J - v(E), \quad (25)$$

for negative  $\xi = x - Vt$ , and  $E(-\infty) = E^{(1)}(J)$ ,  $E(0) = E_-$ . This whole structure (shock and tail region) is called a *monopole with left tail* [5]. Similarly, for  $J \in (J^*, 1)$ , a wavefront joining  $E^{(1)}(J)$  to  $E^{(3)}(J)$  becomes a *monopole with right tail*. This monopole consists of a shock wave having  $E_- = E^{(1)}(J)$ , and  $E_+$  such that  $V(E_+, E^{(1)}(J)) = v(E_+)$ , and a tail region satisfying (25)

for positive  $\xi$ , with the boundary conditions  $E(0) = E_+$  and  $E(\infty) = E^{(3)}(J)$  [5]. In conclusion, the wavefront velocity as a function of  $J$  is determined by the following equations:

$$\begin{aligned} C(J) &= V(E^{(3)}(J), E_-), \text{ with} \\ v(E_-) &= V(E^{(3)}(J), E_-), \text{ if } v_m < J < J^*, \end{aligned} \quad (26)$$

$$\begin{aligned} C(J) &= V(E_+, E^{(1)}(J)), \text{ with} \\ v(E_+) &= V(E_+, E^{(1)}(J)), \text{ if } J^* < J < 1. \end{aligned} \quad (27)$$

Notice that this  $C(J)$  is the limiting value of the rescaled wavefront velocity,  $c(J, \nu)\nu$  as  $\nu \rightarrow 0+$ . We have compared the continuum approximation of the wavefront velocity (in wells traversed per unit time, i.e.,  $c(J, \nu) = C(J)/\nu$ , not rescaled) with the numerical solution of the model for  $\nu = 0.01$  in Fig. 9. The equal-area rule result corresponds to (23), (26) and (27) and its maximum difference with the numerical solution is about 17.6%. Notice that the corrections in Appendix B improve significantly the result: the corrected equal-area result (B2) differs at most 3% from the numerical solution.

*Remark.* A different strategy to derive a formula for the shock velocity  $V(E_+, E_-)$  could be to retain the first order corrections to (22) and then use well-known procedures for partial differential equations. The first-order correction to (22) is

$$\begin{aligned} \frac{\partial E}{\partial t} + v(E) \frac{\partial E}{\partial x} &= J - v(E) \\ + \nu \left( D(E) + \frac{v(E)}{2} \right) \frac{\partial^2 E}{\partial x^2}, \end{aligned} \quad (28)$$

in which terms of order  $\nu^2$  are ignored. As  $\nu \rightarrow 0$ , this equation has shock waves whose velocity obeys the equal-area rule

$$\int_{E_-}^{E_+} \frac{v(E) - V(E_+, E_-)}{D(E) + \frac{v(E)}{2}} dE = 0. \quad (29)$$

instead of (24). Notice that this rule gives the same result as (24) for  $D = 0$ . What is wrong in this argument? Notice that we have to use the rescaled moving variable  $\xi = (x - Vt)/\nu$  to derive (29). After rescaling, both convective and diffusive terms in (28) are the largest ones, of order  $\nu^{-1} \gg 1$ . But so are all the terms in the Taylor series  $(E_i - E_{i-1})/\nu = \partial E/\partial x - (\nu/2) \partial^2 E/\partial x^2 + (\nu^2/6) \partial^3 E/\partial x^3 + \dots$ , which was used to derive (28) in the first place. Thus this derivation ignores infinitely many relevant terms in the Taylor expansions of  $n_i$  and  $n_{i+1}$  and it yields the incorrect formula (29) as a result.

#### IV. CONCLUSIONS

We have analyzed the motion of wavefronts in discrete drift-diffusion models of nonlinear charge transport in superlattices. Moving wavefronts are profiles of the electric

field traveling rigidly with constant velocity. Propagation failure of the fronts occurs because the field profile loses continuity at the critical currents and becomes pinned at discrete sites. We have characterized propagation failure of wavefronts and, conversely, front depinning by singular perturbation methods. These methods are based upon the fact that only a few active wells characterize wavefront motion for dimensionless doping  $\nu$  sufficiently large. In the continuum limit, as  $\nu$  tends to zero, more and more wells become active and a different approximation makes sense. In this limit, discrete equations turn into differential equations, and wavefronts turn into monopoles which are shock waves with a rigid tail region to their left or right. We have derived the equal area rule for such shock waves, and also its leading correction. Our different asymptotic theories perform well in their respective domains of validity and approximate the motion of a wavefront at constant current on an infinite superlattice. Understanding this motion is the key to understanding more sophisticated phenomena occurring in semiconductor superlattices under voltage bias conditions [2,5].

## ACKNOWLEDGMENTS

This work has been supported by the Spanish DGES through grant PB98-0142-C04-01.

## APPENDIX A: DRIFT VELOCITY AND DIFFUSIVITY COEFFICIENTS

To compare our theoretical results with those of numerical solutions of the model, it is better to use analytical approximations of drift velocity and diffusivity instead of using numerical data for them. We use the following dimensionless coefficients which approximately fit those used in Ref. [6]:

$$v(E) = \frac{0.2684 E}{0.25 + (0.9862E - 0.85)^2} + \frac{0.9072}{0.16 + (0.9862E - 15)^2} - 0.004, \quad (\text{A1})$$

$$D(E) = 2 e^{-E^2}. \quad (\text{A2})$$

The velocity has a local maximum at  $E = 1$ ,  $v = 1$ .

## APPENDIX B: FIRST ORDER CORRECTION TO EQUAL-AREA RULE

A more careful derivation of the equal-area rule uses the trapezoid rule for Riemann integrals:

$$\int_{E_-}^{E_+} f(E) dE \approx \sum f(E_i) (E_i - E_{i-1})$$

$$\begin{aligned} & - \frac{1}{2} \sum [f(E_i) - f(E_{i-1})] (E_i - E_{i-1}) \\ & \approx \sum f(E_{i-1}) (E_i - E_{i-1}) \\ & + \frac{1}{2} \sum [f(E_i) - f(E_{i-1})] (E_i - E_{i-1}). \quad (\text{B1}) \end{aligned}$$

We can repeat our derivation in Section III step by step, but keeping now the correction terms (B1) when substituting integrals instead of Riemann sums. The result is

$$V(E_+, E_-) = \frac{\int_{E_-}^{E_+} \frac{v(E)}{v(E)+D(E)} dE + S_N}{\int_{E_-}^{E_+} \frac{dE}{v(E)+D(E)} + S_D}, \quad (\text{B2})$$

$$\begin{aligned} S_N &= \frac{1}{2} \sum \left( \frac{D_i}{v_i + D_i} - \frac{D_{i-1}}{v_{i-1} + D_{i-1}} \right) (E_i - E_{i-1}) \\ &= -\frac{1}{2} \sum \left( \frac{v_i}{v_i + D_i} - \frac{v_{i-1}}{v_{i-1} + D_{i-1}} \right) (E_i - E_{i-1}), \quad (\text{B3}) \end{aligned}$$

$$S_D = \frac{1}{2} \sum \left( \frac{1}{v_i + D_i} - \frac{1}{v_{i-1} + D_{i-1}} \right) (E_i - E_{i-1}). \quad (\text{B4})$$

In the numerator of (B2), we have ignored the term  $\nu \sum (v_i - J)/(v_i + D_i)$ , which vanishes in the continuum limit. Notice that  $v_{i-1} \sim v_i - v'_i (E_i - E_{i-1})$ , a similar relation for  $D_{i-1}$  and that  $v'_i \leq 0$  (typically) and  $D'_i \leq 0$  suggest that  $S_N \leq 0$  and  $S_D \geq 0$ . Thus we expect that the corrected shock velocity be *lower* than the leading order (23).

- 
- [1] H. T. Grahn, R. J. Haug, W. Müller and K. Ploog, Phys. Rev. Lett. **67**, 1618 (1991); J. Kastrup, H. T. Grahn, K. Ploog, F. Prengel, A. Wacker and E. Schöll, Appl. Phys. Lett. **65**, 1808 (1994); J. Kastrup, F. Prengel, H. T. Grahn, K. Ploog and E. Schöll, Phys. Rev. B **53**, 1502 (1996).
  - [2] J. Kastrup, R. Klann, H.T. Grahn, K. Ploog, L.L. Bonilla, J. Galán, M. Kindelan, M. Moscoso, and R. Merlin, Phys. Rev. B **52**, 13761 (1995); J. Kastrup, R. Hey, K.H. Ploog, H.T. Grahn, L. L. Bonilla, M. Kindelan, M. Moscoso, A. Wacker and J. Galán, Phys. Rev. B **55**, 2476 (1997); E. Schomburg, K. Hofbeck, J. Grenzer, T. Blomeier, A. A. Ignatov, K. F. Renk, D.G. Pavel'ev, Yu. Koschurinov, V. Ustinov, A. Zuhov, S. Ivanov and P.S. Kop'ev, Appl. Phys. Lett. **71**, (1997); Y. Zhang, J. Kastrup, R. Klann, K.H. Ploog and H. T. Grahn, Phys. Rev. Lett. **77**, 3001 (1996); K. J. Luo, H. T. Grahn, K. H. Ploog and L. L. Bonilla, Phys. Rev. Lett. **81**, 1290 (1998); J. C. Cao and X.L. Lei, Phys. Rev. B **60**, 1871 (1999).
  - [3] L.L. Bonilla, J. Galán, J.A. Cuesta, F.C. Martínez and J. M. Molera, Phys. Rev. B **50**, 8644 (1994); A. Wacker, in *Theory and transport properties of semiconductor nanostructures*, edited by E. Schöll (Chapman and Hall, New York, 1998). Chapter 10.

- [4] M. Büttiker and H. Thomas, Phys. Rev. Lett. **38**, 78 (1977); A. Sibille, J. F. Palmier, F. Mollot, H. Wang and J.C. Esnault, Phys. Rev. B **39**, 6272 (1989).
- [5] L. L. Bonilla, M. Kindelan, M. Moscoso and S. Venakides, SIAM J. Appl. Math. **57**, 1588 (1997).
- [6] A. Carpio, L. L. Bonilla, A. Wacker and E. Schöll, Phys. Rev. E **61**, 4866 (2000).
- [7] J. P. Keener, SIAM J. Appl. Math. **47**, 556 (1987).
- [8] J.P. Keener and J. Sneyd, *Mathematical Physiology* (Springer, New York, 1998). Chapter 9.
- [9] A. E. Bugrim, A.M. Zhabotinsky and I.R. Epstein, Biophys. J. **73**, 2897 (1997).
- [10] G Grüner, Rev. Mod. Phys. **60**, 1129 (1988); A.A. Middleton, Phys. Rev. Lett. **68**, 670 (1992).
- [11] H. S. J. van der Zant, T. P. Orlando, S. Watanabe and S. H. Strogatz, Phys. Rev. Lett. **74**, 174 (1995); S. Flach and M. Spicci, J. Phys. C **11**, 321 (1999).
- [12] M. Löcher, G.A. Johnson and E.R. Hunt, Phys. Rev. Lett. **77**, 4698 (1996).
- [13] F.R.N. Nabarro, *Theory of Crystal Dislocations* (Oxford University Press, Oxford, 1967).
- [14] P. M. Chaikin and T. C. Lubensky, *Principles of condensed matter physics* (Cambridge University Press, Cambridge, 1995). Chapter 10.
- [15] A. Carpio and L.L. Bonilla, Phys. Rev. Lett. (2001), to appear.
- [16] L. L. Bonilla, G. Platero and D. Sánchez, Phys. Rev. B **62**, 2786 (2000).
- [17] L. L. Bonilla, in *Nonlinear Dynamics and Pattern Formation in Semiconductors and Devices*, edited by F.-J. Niedernostheide (Springer-Verlag, Berlin, 1995), page 1.
- [18] F. J. Higuera and L. L. Bonilla, Physica D **57**, 161 (1992); L. L. Bonilla, I. R. Cantalapiedra, G. Gomila and J. M. Rubí, Phys. Rev. E **56**, 1500 (1997).
- [19] Refs. [5] and [18] consider current self-oscillations mediated by monopoles in SL with  $D = 0$  or by dipoles in the hyperbolic limit of the Gunn effect, respectively. We can use these studies to describe self-oscillations in SL with  $D \neq 0$ . The only thing we need to change is to substitute our equal-area formulas (23) or (B2) instead of the equal-area formulas considered in those papers.
- [20] If we have  $l_n(0) \leq u_n(0)$  such that  $\dot{u}_n \geq D(u_n)(u_{n+1} - 2u_n + u_{n-1})/\nu - v(u_n)(u_n - u_{n-1})/\nu + J - v(u_n)$ , and  $l_n \leq D(l_n)(l_{n+1} - 2l_n + l_{n-1}) - v(l_n)(l_n - l_{n-1})/\nu + J - v(l_n)$ , then  $l_n(t) \leq u_n(t)$  for all later times.  $l_n(t)$  and  $u_n(t)$  are called sub and supersolutions, respectively. See Ref. [6]. The use of comparison principles is restricted to spatially discrete or continuous differential equations which are first order in time. For applications to parabolic partial differential equations, see M.H. Protter and H.F. Weinberger, *Maximum principles in differential equations* (Springer, New York, 1984).
- [21] A. Carpio, S.J. Chapman, S. Hastings, J.B. McLeod, Eur. J. Appl. Math. **11**, 399 (2000).
- [22] S. Flach, Y. Zolotaryuk and K. Kladko, Phys. Rev. E **59**, 6105 (1999). See paragraph below Eq. (27).
- [23] B. Zinner, J. Diff. Eqs. **96**, 1 (1992); A.-M. Filip and S. Venakides, Comm. Pure Appl. Math. **52**, 693 (1999).
- [24] L. L. Bonilla, J. Statist. Phys. **46**, 659 (1987).
- [25] B. W. Knight and G. A. Peterson, Phys. Rev. **147**, 617

(1966); J. D. Murray, J. Fluid Mech. **44**, 315 (1970).

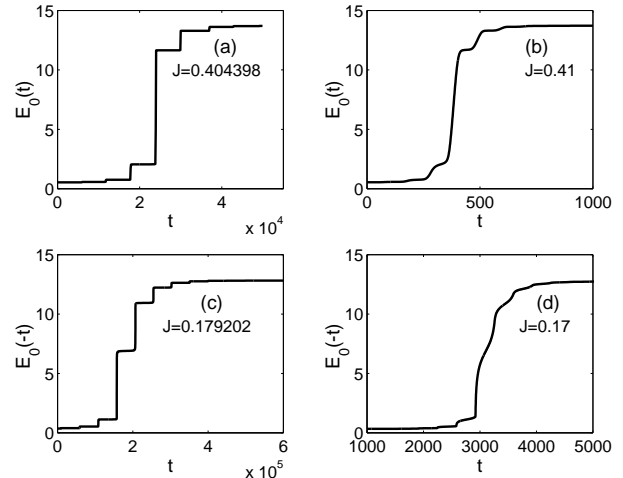


FIG. 1. Sharpening of wavefront profiles as the dimensionless current  $J$  approaches its critical values for  $\nu = 3$ . (a)  $J \approx J_2$ , (b)  $J > J_2$ , (c)  $J \approx J_1$ , (d)  $J < J_1$ .

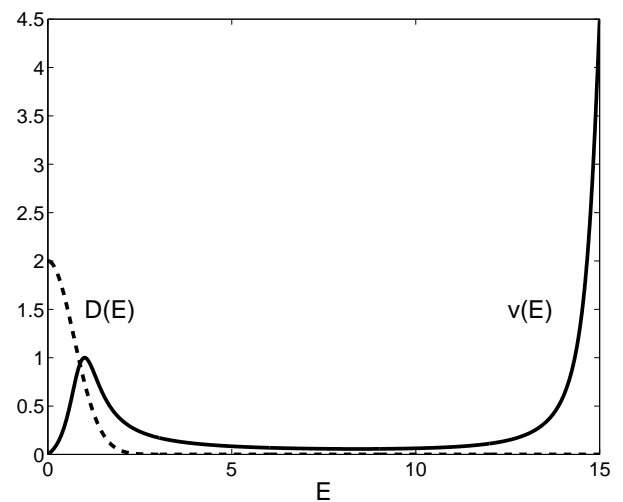


FIG. 2. Electron drift velocity  $v(E)$  and diffusion coefficient  $D(E)$  as functions of the electric field in nondimensional units.

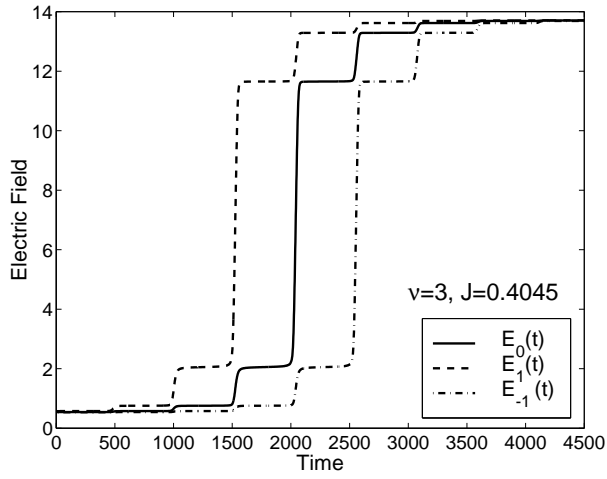


FIG. 3. Electric field profile of a wavefront at three consecutive wells. We have depicted the field at each well as a function of time, which illustrates the motion of the front at constant velocity.

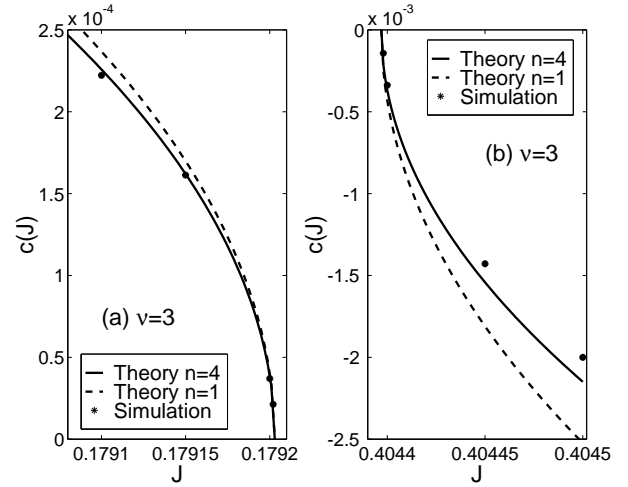


FIG. 5. Wavefront velocity as a function of current density for  $\nu = 3$ . We have compared the numerically measured velocity to the results of our theory with one or four active wells.

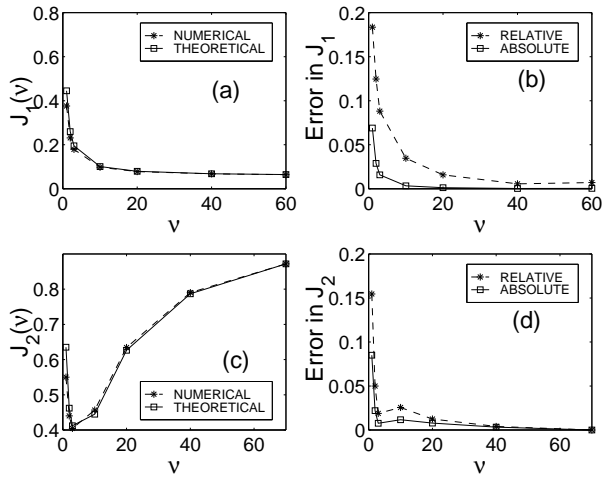


FIG. 4. Upper and lower critical currents as functions of the dimensionless  $\nu$ .

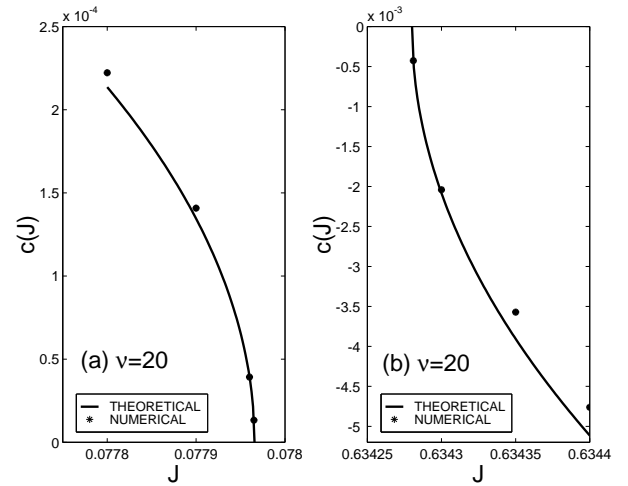


FIG. 6. Wavefront velocity as a function of current density for  $\nu = 20$ . We have compared the numerically measured velocity to the results of our theory with one active well.

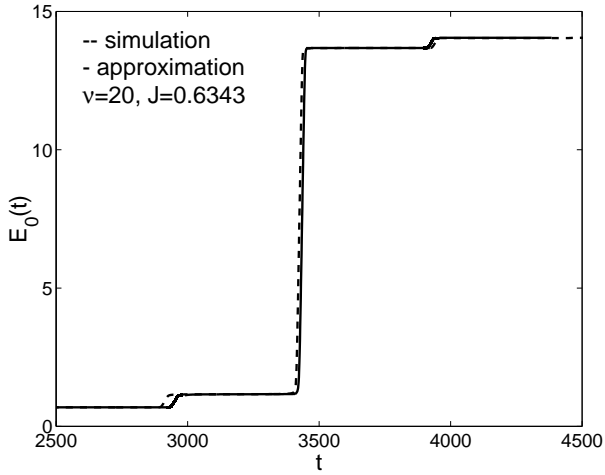


FIG. 7. Wavefront profiles near  $J = J_2$  for  $\nu = 20$ . We compare the results of matched asymptotic expansions with one active well and the numerical solution of the model.

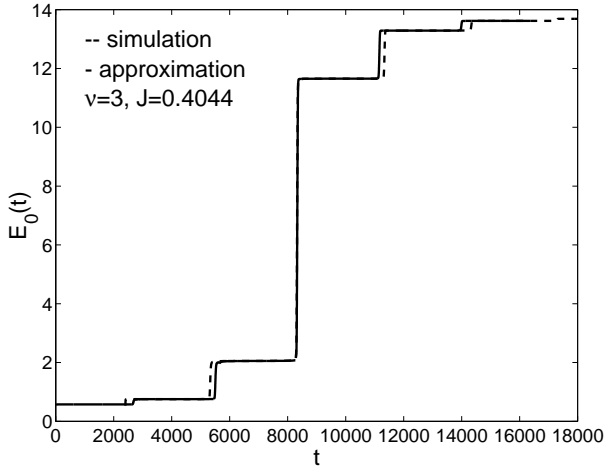


FIG. 8. Wavefront profiles near  $J = J_2$  for  $\nu = 3$ . We compare the numerical solution of the model with the result of matched asymptotic expansions with 5 active wells. Notice that the largest error source is the theoretical estimate of the time period (an error of 200 in a 3,000 period).

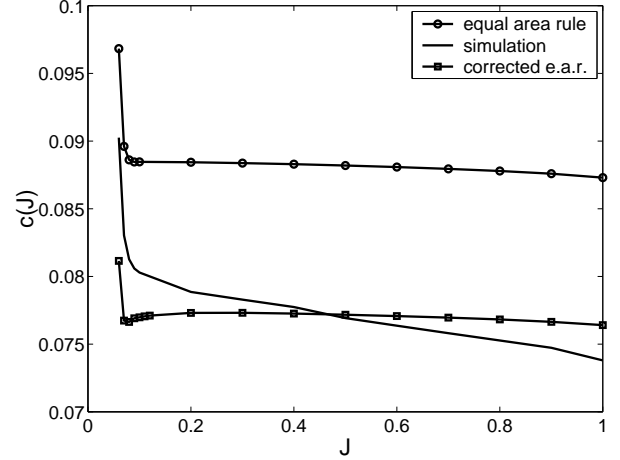


FIG. 9. Comparison of the equal-area rule (leading order) and corrected equal-area rule (including first order corrections) approximations to the wavefront velocity with the numerical solution of the model for  $\nu = 0.01$ .